In Vivo Longitudinal Tracking of Lymphangiogenesis and Angiogenesis in Cutaneous Melanoma Mouse Model Using Multifunctional Optical Coherence Tomography

Pei-Yu Lai[1,2], Tai-Yu Shih[1,2], Yu-Huan Chang[1,2], Ya-Shuan Chou[3,4], Ting-Hua Wu[3], Yu-Ya Su[3,4], Chung-Hsing Chang[3,4,5,6] and Wen-Chuan Kuo[1,2]

Melanoma is a high-risk skin cancer because it tends to metastasize early and ultimately leads to death. In this study, we introduced a noninvasive multifunctional optical coherence tomography (MFOCT) for the early detection of premetastatic pathogenesis in cutaneous melanoma by label-free imaging of microstructures (i.e., providing the thickness and the scattering information) and microcirculation (i.e., providing depth-resolved angiography and lymphangiography). Using MFOCT-based approaches, we presented an in vivo longitudinal observation of the tumor microenvironment in *Braf* $^{V600E/V600E}$;*Pten* $^{-/-}$ mice with inducible melanoma monitored for 42 days. Quantitative analysis of MFOCT images identified an increased number of lymphatic and vascular vessels during tumor progression and faster lymphangiogenesis (beginning on day 21) than angiogenesis (beginning on day 28) in the melanoma microenvironment. We further observed lymphatic vessel enlargement from the first week of melanoma development, implying tumor cells interacting with the vessels and increased likelihood of metastasis. MFOCT identified cutaneous melanoma–associated angiogenesis and lymphangiogenesis before the possible visual perception of the tumor (≥42 days) and before metastasis could be diagnosed using micropositron emission tomography (35 days). Thus, the proposed quantitative analysis using MFOCT has the potential for early detection of cutaneous melanoma progression or prediction of metastatic melanoma in a mouse model. However, retrospective and extensive experiments still need to be performed in the future to confirm the value of MFOCT in clinical application.

JID Innovations (2021);**1:**100010 doi:10.1016/j.xjidi.2021.100010

INTRODUCTION

Melanoma is not a common type of skin cancer. Nevertheless, it accounts for most of the deaths among patients with cutaneous tumors because it tends to spread to vital organs of the body. Reducing the likelihood of mortality is principally achieved through the early identification of patients who have a high risk of developing metastasis. In clinical practice, patients with melanoma are staged according to their Clark level, Breslow thickness, primary tumor ulceration, mitotic activity, and sentinel lymph node (LN) biopsy (Leachman et al., 2016). Several studies have discovered that increased Breslow thickness is an indicator of sentinel LN metastasis in patients with melanoma (Cadili and Dabbs, 2010; McMasters et al., 2001; Paek et al., 2007).

Nonetheless, metastasis does occur in some patients with melanoma tumors <1 mm thick (Morton et al., 2003). Although no highly specific predictive factors of metastatic melanoma have yet been identified, melanoma is known to induce angiogenesis (Streit and Detmar, 2003), and metastasis is known to spread mostly through the lymphatic vessels (Doeden et al., 2009; Storr et al., 2012). Lymphangiogenesis has been correlated with LN metastasis and patient survival (Dadras et al., 2003; Emmett et al., 2010; Massi et al., 2006; Shayan et al., 2012), indicating that lymphangiogenesis is a better indicator of whether tumor had become metastatic than the current measurement of the tumor thickness (Dadras et al., 2005). Tumor-associated lymphatic vessels have emerged as a valid therapeutic target for controlling metastatic disease, and the first specific antilymphangiogenic drugs have recently entered clinical testing (Dieterich and Detmar, 2016).

However, imaging the lymphatic system is difficult because the lymphatic vessels transport mostly lymph and carry a few cells. Hence, a contrast agent must be

[1]*Institute of Biophotonics, National Yang Ming Chiao Tung University, Taipei, Taiwan;* [2]*Institute of Biophotonics, National Yang-Ming University, Taipei, Taiwan;* [3]*Skin Institute, Hualien Tzu Chi Hospital, Hualien, Taiwan;* [4]*Regenerative Medicine and Cell Therapy Research Center, Kaohsiung Medical University, Kaohsiung, Taiwan;* [5]*Institute of Medical Sciences, Tzu Chi University, Hualien, Taiwan; and* [6]*Research Center for Applied Sciences, Academia Sinica, Taipei, Taiwan*

Correspondence: Wen-Chuan Kuo, Institute of Biophotonics, National Yang-Ming University, Taipei 112, Taiwan. E-mail: wckuo@ym.edu.tw or kuo@nycu.edu.tw

Abbreviations: 3D, three-dimensional; 4-HT, (Z)-4-hydroxytamoxifen; CT, computed tomography; LN, lymph node; MFOCT, multifunctional optical coherence tomography; OCT, optical coherence tomography; PET, positron emission tomography

Received 2 November 2020; revised 12 February 2021; accepted 15 February 2021; accepted manuscript published online 18 March 2021; corrected proof published online 23 April 2021

Cite this article as: JID Innovations 2021;1:100010

administered in most imaging techniques. The noninvasive visualization techniques currently used clinically include computed tomography (CT), positron emission tomography (PET), magnetic resonance imaging, and near-infrared fluorescence imaging (Eklund et al., 2013; Munn and Padera, 2014). The uptake of ^{18}fluorodeoxyglucose into cancer cells, which have a higher demand for glucose than noncancer cells, can be detected using PET. The integration of PET and CT is often employed in LN staging (Seo et al., 2014; Takenaka et al., 2012). Magnetic resonance imaging can be used to assess lymphatic vessels and LNs with or without the injection of a contrast agent. Although the field of view and penetration depth of PET, CT, and magnetic resonance imaging are sufficient, imaging of capillaries using these techniques is impossible owing to low spatial resolution. Near-infrared imaging using indocyanine green has been employed to image the lymphatic system, but indocyanine green was found to alter lymph transport in vivo (Gashev et al., 2010). The techniques listed earlier have been used in several clinical and preclinical research, but each has certain limitations.

Consequently, advanced approaches are needed, such as optical coherence tomography (OCT). OCT provides a noninvasive, depth-resolved, nondestructive imaging at a higher resolution, and follow-up assessment with OCT images may add subsurface three-dimensional (3D) information. Vakoc et al. (2009) pioneered OCT lymphangiography using intrinsic contrast caused by the weak scattering of lymph relative to that of the surrounding tissue. OCT lymphangiography has since been used to track inflammation (Qin et al., 2015) and the wound healing process (Yousefi et al., 2014).

In this study, we introduced a quantitative multifunctional OCT (MFOCT), explored the capability of MFOCT to display the network structure of blood vessels and lymphatic vessels in the ears of a mouse with spontaneously induced cutaneous melanoma, and compared its use with that of PET in detecting prognostic microstructural markers that could predict early metastasis to the lymphatics. Our findings reveal the potential benefit of MFOCT in simultaneously imaging depth-resolved microstructures and microcirculation through contrast-free angiography and lymphangiography.

RESULTS

Histopathology and S100 immunohistochemistry of melanoma samples

The time-course study of the histopathology of melanoma on *Braf* $^{V600E/V600E}$;*Pten*$^{-/-}$ mouse ears is illustrated in Figure 1. In normal mouse ear skin, pigmented melanocytes scatter in the dermis (day 0). Pigmented cells increase in number and gather to form patches in the dermis (day 21); thickening of the dermis with increased fibrosis and vessels (day 28) are noted during melanomagenesis. In advanced melanoma (day 42), pigmented cells infiltrate diffusely in the dermis with loss of adipose tissue. To characterize the nonpigmented tumor, we stained it using a melanocyte marker (S100) and confirmed that the tumors were composed of S100-positive cells, indicating nonpigmented melanoma in the *Braf* $^{V600E/V600E}$;*Pten*$^{-/-}$ mouse ear (Figure 2). The histological pictures provided a reference map for the parallel MFOCT study.

Microstructure change

An MFOCT cross-sectional in vivo image of a normal mouse ear parallel with its H&E and S100 staining is shown in Figure 3a where the epidermis, dermis, and cartilage are visible because of the various scattering properties of each tissue type. The microstructure features in the image correspond to the standard histology. In the advanced stage of melanoma (i.e., on day 56), strong scattering regions within the tissue, indicated with yellow arrows, as seen in Figure 3b, correspond to the dense infiltration of S100-positive melanoma cells in the dermis. A 3D reconstruction of a *Braf* $^{V600E/V600E}$;*Pten*$^{-/-}$ mouse ear (on day 56) is shown in Figure 3c. We reduced the 3D-reconstructed image of the mouse ear to the enface maximum intensity projection and inverted the grayscale (Figure 3e). White areas in the maximum intensity projection are artifacts caused by the reflection from the optical gel, which was used to maintain the skin moisture and eliminate the strong back reflection of light from the skin surface. The condensed black dots in the maximum intensity projection map indicate the tumor locations and correspond to the strongly scattered signals in the OCT 3D reconstruction (Figure 3c), similar to that in the corresponding photograph (Figure 3d).

Figure 3f shows a photograph and corresponding thickness map of a *Braf* $^{V600E/V600E}$;*Pten*$^{-/-}$ mouse ear on day 42. No direct correlation can be observed between the surface black dots and the thickness map because a part of the melanoma cells is amelanotic and may not be observed in photographs. This implies that only seeing the skin surface is indeed a limitation of visual inspection. We also evaluated tissue thickness changes in the same region of the ear at different time points. The bar chart in Figure 3g statistically summarizes this quantitative result, indicating a significant difference in the measured ear thickness between the *Braf* $^{V600E/V600E}$;*Pten*$^{-/-}$ and *Braf* $^{CA/CA}$;*Pten*$^{loxp/loxp}$ mice only on day 42 ($P < 0.05$).

Lymphangiogenesis and angiogenesis

Alteration of the microvascular and lymphatic dynamics (intensity, diameter, tortuosity) was perceived at the early stage of *Braf* $^{V600E/V600E}$;*Pten*$^{-/-}$ mice with melanoma. Although no tumor lesion could be visualized on the skin surface after 7 days of treatment with (Z)-4-hydroxytamoxifen (4-HT) (Figure 4a), lymphangiogenesis was clearly observed using OCT lymphangiography (Figure 4b). In comparing each time point with the baseline, significant differences were found (indicated with the plus sign $^{+}$ in Figure 4c) in lymphatic density on day 21 ($P < 0.01$), day 28 ($P < 0.01$), day 35 ($P < 0.01$), and day 42 ($P < 0.05$). Furthermore, significant increases in the lymphatic vessel diameter of the *Braf* $^{V600E/V600E}$;*Pten*$^{-/-}$ mice were observed on day 7 ($P < 0.05$), day 14 ($P < 0.01$), day 21 ($P < 0.01$), day 28 ($P < 0.01$), and day 42 ($P < 0.01$). Increases in lymphatic vessel tortuosity of the *Braf* $^{V600E/V600E}$;*Pten*$^{-/-}$ mice were also significant on day 14 ($P < 0.05$), day 21 ($P < 0.01$), day 28 ($P < 0.01$), day 35 ($P < 0.01$), and day 42 ($P < 0.01$). We observed significant differences in lymphatic density (indicated with asterisk *) between *Braf* $^{V600E/V600E}$;*Pten*$^{-/-}$ mice and control *Braf* $^{CA/}$

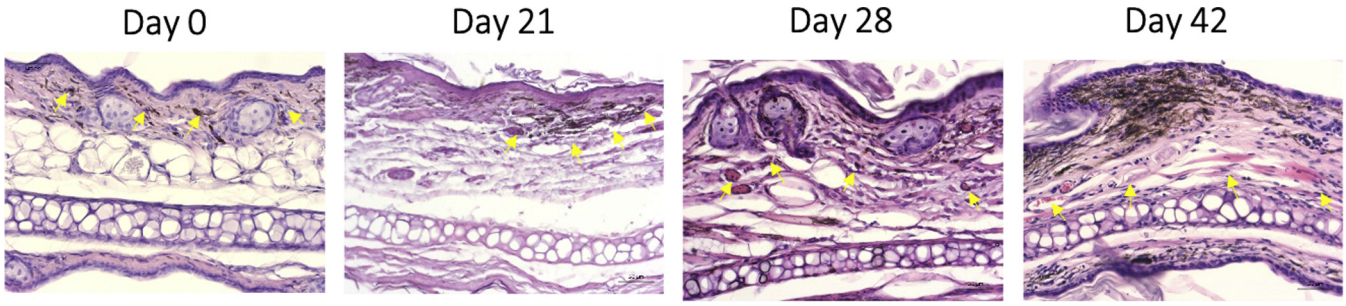

Figure 1. Time-course study of histopathology of melanoma on *Braf*$^{V600E/V600E}$;*Pten*$^{-/-}$ mouse ears. In normal mouse ear skin, pigmented melanocytes scatter in the dermis (day 0). Pigmented cells increase in number and gather to form patches in the dermis (day 21); thickening of the dermis with increased fibrosis and vessels (day 28) are noted during melanomagenesis. In advanced melanoma (day 42), pigmented cells infiltrate diffusely in the dermis with a loss of adipose tissue.

^{CA};*Pten*$^{loxp/loxp}$ mice on day 21 ($P < 0.01$), day 28 ($P < 0.01$), day 35 ($P < 0.05$), and day 42 ($P < 0.01$). Lymphatic vessel diameters were also significantly different in these mice on day 7 ($P < 0.05$), day 14 ($P < 0.01$), day 21 ($P < 0.01$), day 28 ($P < 0.01$), and day 42 ($P < 0.01$). The lymphatic vessel tortuosity of the *Braf* $^{V600E/V600E}$;*Pten*$^{-/-}$ mice was higher at all time points than that of the *Braf*$^{CA/CA}$;*Pten*$^{loxp/loxp}$ control mice, with significant differences observed on day 21 ($P < 0.01$) and day 28 ($P < 0.01$) (Figure 4c).

Changes caused by angiogenesis in the vascular network were smaller than the changes caused by lymphangiogenesis before day 28, but remarkable angiogenesis was observed from day 28 to day 42 (Figure 5b). The newly formed vessels were small and curved compared with the existing vessels and had an average diameter of ~9 μm, as measured using ImageJ software (National Institutes of Health, Bethesda, MD) (Schneider et al., 2012). A significant difference in the blood vessel density between each time point and the baseline was seen on day 7 ($P < 0.05$), day 28 ($P < 0.01$), day 35 ($P < 0.01$), and day 42 ($P < 0.01$). In addition, a significant increase in blood vessel tortuosity was observed on day 14 ($P < 0.05$), day 28 ($P < 0.01$), day 35 ($P < 0.01$), and day 42 ($P < 0.01$) compared with that at baseline. In comparison with that of the control *Braf* $^{CA/CA}$;*Pten*$^{loxp/loxp}$ mice, a significant difference in blood vessel density was observed on day 28 ($P < 0.01$), day 35 ($P < 0.01$), and day 42 ($P < 0.01$). We also observed a significant difference in blood vessel tortuosity on day 35 ($P < 0.01$) and day 42 ($P < 0.05$). However, no significant increase in blood vessel diameter was observed comparing each time point with the baseline or comparing with the control mice (Figure 5c).

Coregistration of lymphangiography and angiography showed that lymphangiogenesis did not occur in parallel with angiogenesis (Figure 6a). The change in the distribution of lymphatic capillaries occurred earlier on day 7. We employed the MFOCT system to observe tumors with amelanotic melanoma (Figure 6b, lower row, day 35), as confirmed with S100 protein staining of histological sections at the endpoint of the experiment (Figure 2). Lymphatic and blood vessels surrounding the tumor can be observed in both pigmented melanoma and amelanotic melanoma, which implies that patterns of lymphangiogenesis and angiogenesis are not affected by pigmentation. In contrast to the ear of the mice with a tumor, the coregistration of lymphangiography and angiography in control *Braf* $^{CA/CA}$;*Pten*$^{loxp/loxp}$ mice ear from day 0 to day 42 shows no significant pattern changes (Figure 7).

The microPET imaging is shown in Figure 8a, using ^{18}fluorodeoxyglucose amassments in the cervical LN of one representative *Braf* $^{V600E/V600E}$;*Pten*$^{-/-}$ mouse on days 21, 28, and 35. Details of the rectangular regions (upper row) are enlarged (lower row). White arrows indicate the cervical LNs on the PET-CT images. Uptake of ^{18}fluorodeoxyglucose was higher in the cervical LN on days 28 and 35 than on day 21. Quantitative analysis using the average from three mice yielded the mean uptake in the cervical LNs relative to that in the leg versus time (Figure 8b). A significant difference was observed between day 21 and day 35 ($n = 3$, $P < 0.05$), indicating that metastasis may occur around day 35. MFOCT was able to detect the lymphatic changes in cutaneous melanoma much earlier than the LN changes detected by PET scan.

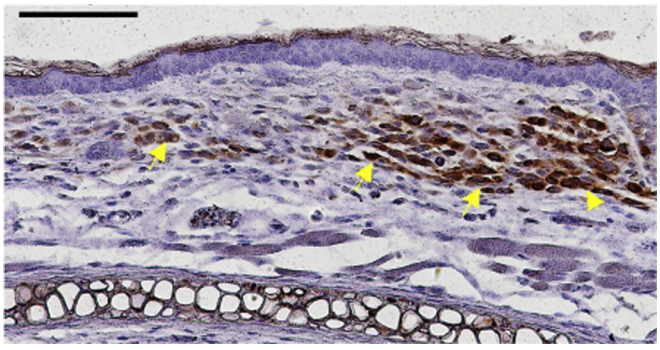

Figure 2. Immunohistochemistry of S100 on a nonpigmented tumor of a *Braf*$^{V600E/V600E}$;*Pten*$^{-/-}$ mouse ear. S100-positive cells were shown in the dermis, which indicates that the tumor is composed of nonpigmented melanoma cells. Bar = 100 μm.

DISCUSSION

OCT provides a noninvasive, depth-resolved, nondestructive imaging at a higher resolution than ultrasonography and a deeper imaging depth than confocal microscopy and can add subsurface 3D information during follow-up assessment. Since 1997, OCT has been applied in dermatology and is now employed in much clinical skin research (Baran et al., 2016; Gong et al., 2014; Pomerantz et al., 2011; Welzel et al., 2003). Although histological examination of

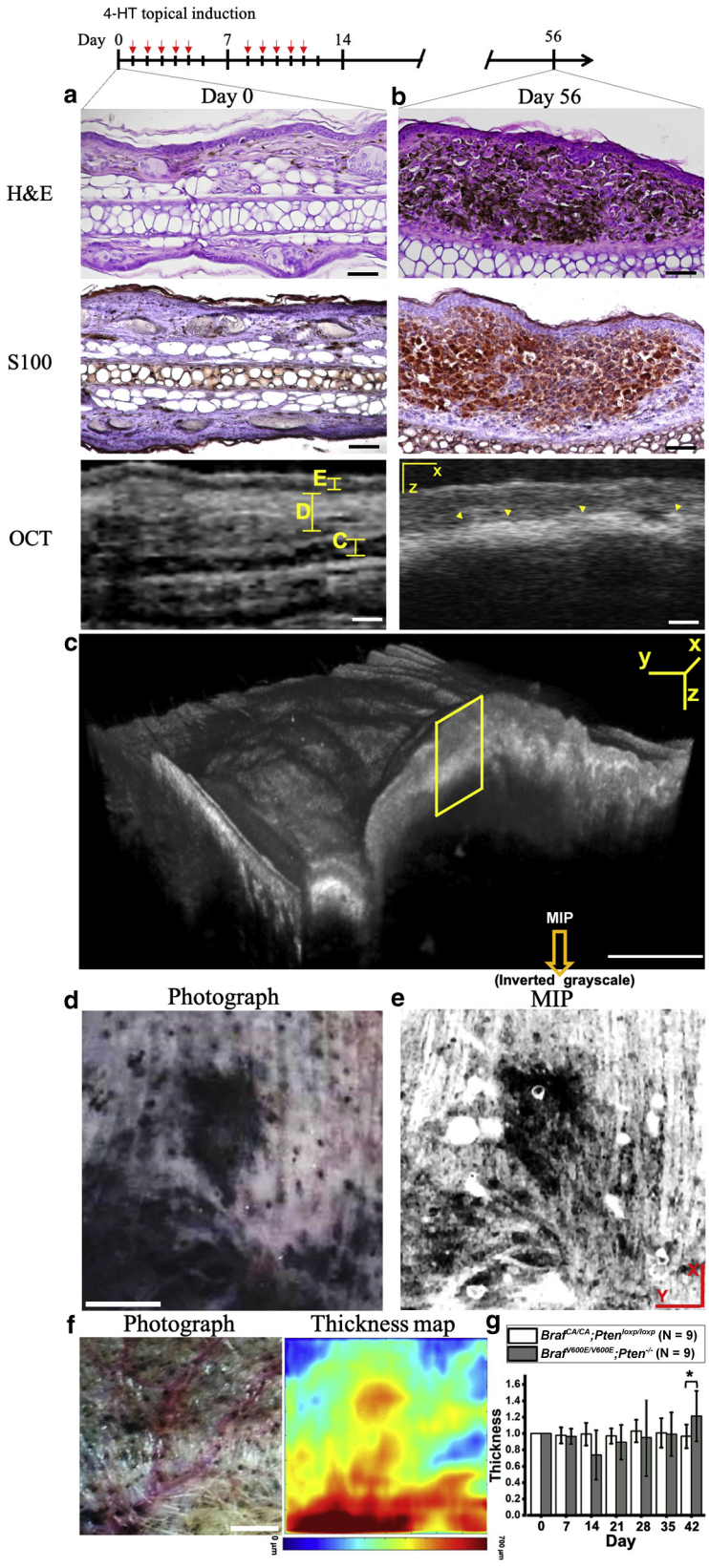

Figure 3. MFOCT shows the microstructure, 3D reconstruction, thickness, and scattering analysis in *Braf* $^{V600E/V600E}$;*Pten*$^{-/-}$ mouse ear. H&E, S100-stained section, and MFOCT cross-sectional in vivo image of (**a**) control and (**b**) *Braf* $^{V600E/V600E}$;*Pten*$^{-/-}$ mouse ear (day 56). Yellow arrows point to the strong scattering region. Bar = 50 μm. (**c**) 3D reconstruction of MFOCT cross-sectional images; area of the yellow rectangle corresponds to **b**. Bar = 1 mm. (**d**) Photograph and (**e**) corresponding MIP of the area in **c** (inverted grayscale). Bar = 1 mm. (**f**) Photograph and corresponding thickness map of a *Braf* $^{V600E/V600E}$;*Pten*$^{-/-}$ mouse ear (day 42). Bar = 1 mm. (**g**) Measured tissue thickness in the same region of the ear at different time points. Statistical significance was evaluated between *Braf* $^{V600E/V600E}$;*Pten*$^{-/-}$ mice and control *Braf* $^{CA/CA}$;*Pten*$^{loxp/loxp}$ mice using the two-sided *t*-test. $*P < 0.05$. Quantitative results were conducted on the same scanned areas at different time points. N represents the number of scanned areas. 3D, three-dimensional; 4-HT, (Z)-4-hydroxytamoxifen; C, cartilage; D, dermis; E, epidermis; MFOCT, multifunctional optical coherence tomography; MIP, maximum intensity projection.

skin lesion remains the gold standard for diagnosis, performing biopsies on all skin lesions are not feasible. Finding the correct lesion(s) to perform a biopsy on in a patient with many pigmented lesions is still a challenge. Besides, the specificity of visual inspection of lesions by the ABCD criteria (Asymmetry; Border; Color; Diameter or Dark) varies widely based on the experience of the clinician (Thomas et al., 1998).

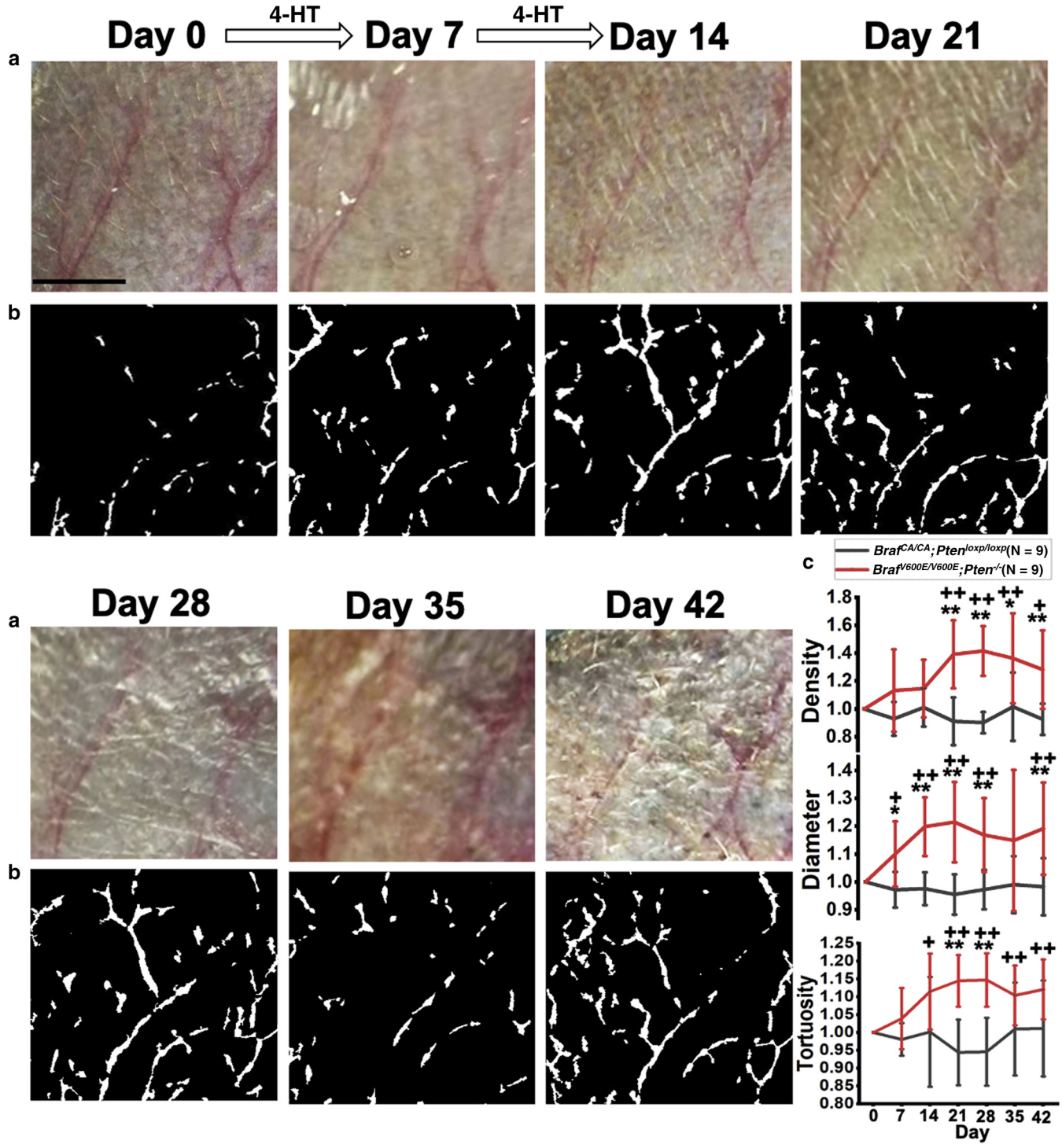

Figure 4. Longitudinal tracking of lymphangiography employed surface vascular features as landmarks for registration across time points in *Braf*$^{V600E/V600E}$;*Pten*$^{-/-}$ mouse ears. Changes in lymphatic area density are evident after 21 days of 4-HT administration, whereas changes in diameters are evident after 7 days of 4-HT administration. (**a**) Photograph, (**b**) lymphangiography, and (**c**) quantitative analysis of lymphatic vessel networks in vivo, revealing lymphangiogenesis during melanoma progression. Quantitative results were obtained from the same scanned areas at different time points, and values were normalized to those on day 0. Statistical significance was evaluated between (i) each time point and the baseline (indicated with plus sign $^{+}$) and between (ii) *Braf*$^{V600E/V600E}$;*Pten*$^{-/-}$ mice and control *Braf*$^{CA/CA}$;*Pten*$^{loxp/loxp}$ mice (indicated with asterisk *) using the two-sided *t*-test. $^{+}P < 0.05$; $^{++}P < 0.01$; $^{*}P < 0.05$; $^{**}P < 0.01$. N represents the number of scanned areas. Bar = 1 mm. 4-HT, (Z)-4-hydroxytamoxifen; MFOCT, multifunctional optical coherence tomography.

In this work, we obtained subsurface information that indicated that advanced melanoma (on day 56) caused strong scattering in the MFOCT image and perceived an increase in quantitative ear thickness. On the basis of light–tissue interaction theories (Bohren and Huffman, 1983), the strong scattering characteristics and the increase of the ear thickness in MFOCT images may be due to the significant variation of refractive indices in malignant

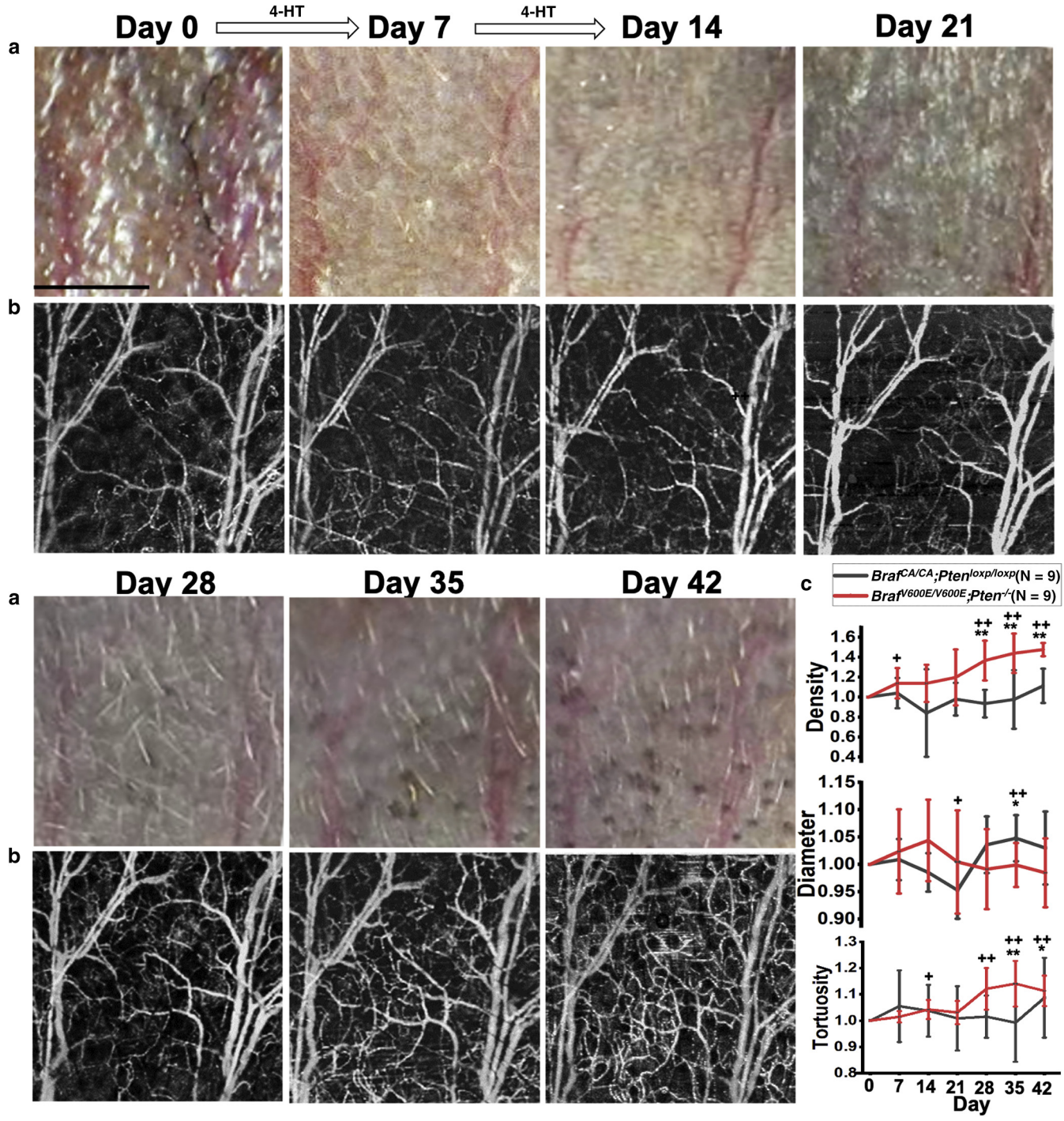

Figure 5. Longitudinal tracking of blood vessels using MFOCT in a *Braf*$^{V600E/V600E}$;*Pten*$^{-/-}$ mouse ear. Angiogenesis is evident after day 28. (**a**) Photograph, (**b**) angiography, and (**c**) quantitative analysis of vascular networks in vivo, revealing angiogenesis during melanoma progression. Quantitative results were obtained from the same scanned areas at different time points, and values were normalized to those on day 0. Statistical significance was evaluated between (i) each time point and the baseline (indicated with the plus sign $^{+}$) and between (ii) *Braf*$^{V600E/V600E}$;*Pten*$^{-/-}$ mice and control *Braf* $^{CA/CA}$;*Pten*$^{loxp/loxp}$ mice (indicated with asterisk *) using the two-sided *t*-test. $^{+}P<0.05$; $^{++}P<0.01$; $^{*}P<0.05$; $^{**}P<0.01$. N represents the number of scanned areas. Bar = 1 mm. 4-HT, (Z)-4-hydroxytamoxifen; MFOCT, multifunctional optical coherence tomography.

tissues with increased concentration of melanocytes and cell size (Turani et al., 2019), as shown in our time-course results of histopathology in melanoma mouse ear (Figure 1). Because an increase in the number of melanocytes and in the number of cells with pleomorphic nuclei is the hallmark of melanoma on pathological assessment (Rhodes et al., 1983), the scattering information obtained by MFOCT can help locate tumor locations in a 3D fashion (Figure 3c–e). Melanoma can be differentiated from healthy tissue using maximum intensity projection images or thickness maps when the surface-visible melanoma area is $\geq$1 mm^2.

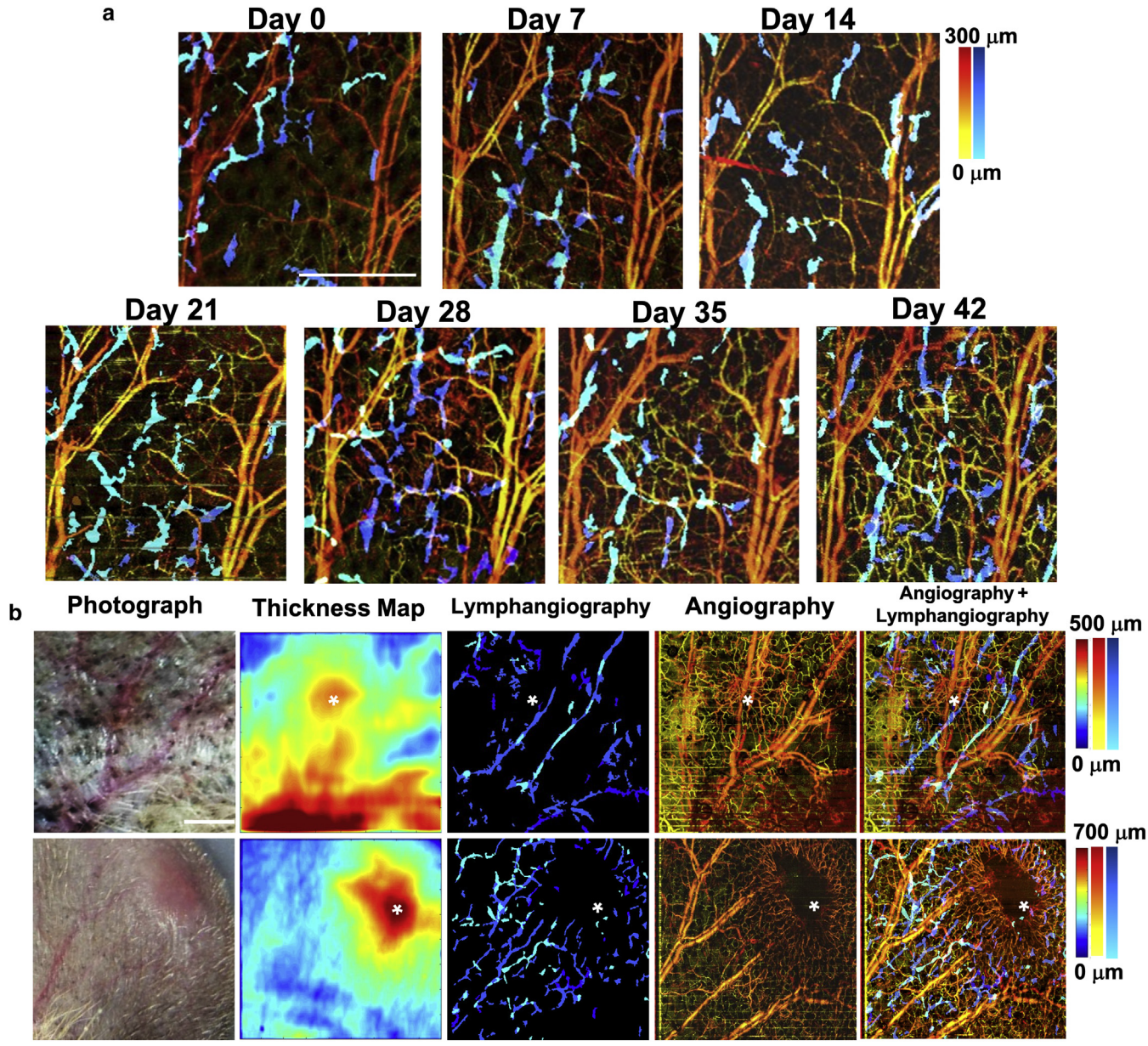

Figure 6. Coregistration of lymphangiography (blue color bar) and angiography (red color bar) reveals that lymphangiogenesis does not occur in parallel with angiogenesis. Newly formed lymphatic (inner) and blood (outer) vessels surrounding the tumor can be observed in densely distributed melanoma and amelanotic melanoma. (**a**) Monitoring of the angiography and lymphangiography within the *Braf* $^{V600E/V600E}$*;Pten* $^{-/-}$ mouse ear. (**b**) Photograph, thickness map, MFOCT lymphangiography, MFOCT angiography, and MFOCT angiography merged with MFOCT lymphangiography of the ear of the mice with melanoma (upper row) and those with amelanotic melanoma (lower row). Bar = 1 mm. MFOCT, multifunctional optical coherence tomography.

We also observed vascular network changes during cancer progression, with a significant increase in vessel density that began on day 28. The newly formed small vessels had a more tortuous vessel trajectory than those in the normal skin (day 0), indicating that angiogenesis had begun before metastasis could be identified using microPET (day 35), even before visual inspection of the tumor (≥42 days). When comparing these parameters with those of the control group, a significant difference was found after day 28 in blood vessel density and after day 35 in blood vessel tortuosity. However, the change in vessel diameter was less prominent than that in vessel density and tortuosity.

Contrary to the vascular pattern, the number of lymphatic vessels began to increase on day 21. Lymphatic vessel diameter started to increase on day 7. The lymphatic vessel tortuosity began to increase on day 14 and lasted until day 42, indicating that lymphangiogenesis does not parallel with angiogenesis. We also observed a significant difference between *Braf* $^{V600E/V600E}$*;Pten* $^{-/-}$ and *Braf* $^{CA/CA}$*;Pten* $^{loxp/loxp}$ in lymphatic density after day 21 and in lymphatic vessel diameter after day 7. Among these parameters, lymphatic enlargement was the most sensitive indicator of tumor lymphangiogenesis and could be a prognostic marker for predicting whether tumors are metastatic to sentinel LNs.

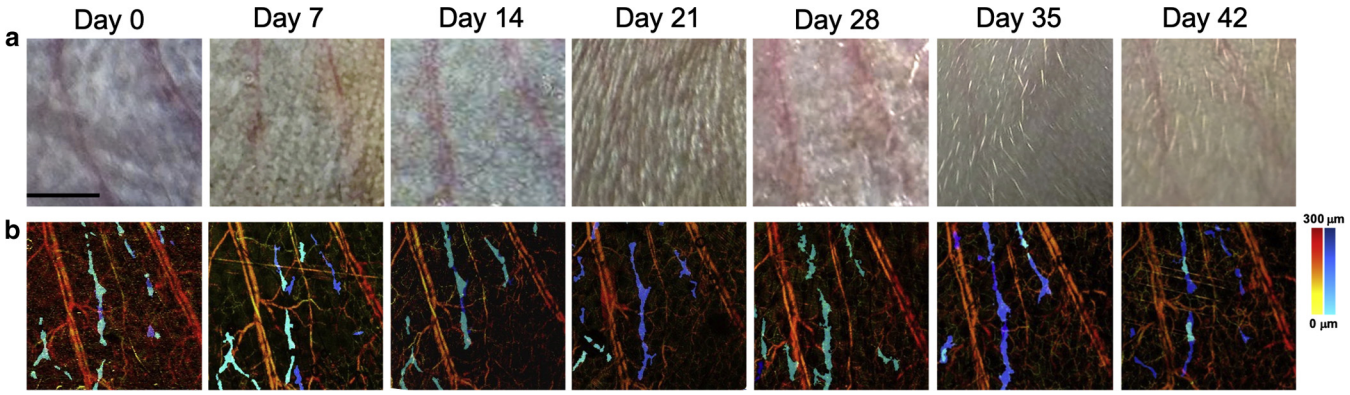

Figure 7. Coregistration of lymphangiography (blue color bar) and angiography (red color bar) of the ear of *Braf*$^{CA/CA}$;*Pten*$^{loxp/loxp}$ control mice from day 0 to day 42. The blood vessels and lymphatic ducts are differentially expressed in the images without significant change in the pattern during the time-course study. (**a**) Photograph. (**b**) MFOCT angiography merged with MFOCT lymphangiography of the control mouse ear. Bar = 1 mm. MFOCT, multifunctional optical coherence tomography.

The development of melanoma in the mouse model we used has been previously reported with short latency and metastases observed in LN and lungs (Dankort et al., 2009). In that study, mice were killed on ~day 49 after the detection of the presence of malignant melanoma lesions, assessed by visual inspection of the underside of the ventral and the lateral skin. Our experiment found malignant melanoma lesions at dorsal skin around day 42, implying that tumor metastasis happened before day 42. PET-CT imaging also found increased uptake of ^{18}fluorodeoxyglucose in the cervical LNs of mice, indicating that tumor metastasis may occur around day 35. Besides, our quantitative MFOCT result shows a rapid increase in lymphatic diameter (20%) and density (40%) around days 14 and 21 compared with that at the baseline, with a relative increase of ~20% and ~30%, respectively, on day 42. The results discussed earlier indicated that the lymphatic diameter and density on days 14 and 21 were nearly the same as those at the time point when the metastasis occurred. Therefore, from these quantitative results, we may conclude that lesions with a relative increase in lymphatic vessel density and diameter above 20% can be considered high-risk metastatic.

Nevertheless, lymphangiogenesis is not specific for metastatic melanoma. Inflammatory skin diseases that can be characterized as acute or chronic also induce lymphangiogenesis. Acute inflammation is a short-term process occurring in response to tissue injury (Baran et al., 2016). This finding is different from our observation of tumor metastasis with persistent lymphangiogenesis lasting from day 7 through day 42. Other chronic inflammatory skin diseases, such as dermatitis (eczema), rosacea (Rainer et al., 2017), seborrheic dermatitis, and psoriasis, may also induce lymphangiogenesis; however, these diseases are easily distinguished from melanoma by appearance and symptoms (Borda and Wikramanayake, 2015; Kim et al., 2017; McPherson, 2016; Rainer et al., 2017).

Some limitations are evident in applying MFOCT in the clinic. First, penetration depth in MFOCT images will be affected when heavy pigmentation exists, as shown in Figure 3b. Therefore, observing melanoma-associated angiogenesis and lymphangiogenesis in the dermis seems to be only feasible in patients with early-stage melanoma. Second, lymphangiogenesis is a relevant predictor only if it follows suspicious skin lesions over time. Besides, comparing the suspicious skin regions with nearby healthy tissues may also be needed to suggest characteristic lymphangiogenesis. Third, human participants are required to establish a cut-off value of lymphangiogenesis to achieve clinical utility.

In summary, using MFOCT in murine cutaneous melanoma, our findings indicate that the detection of lymphangiogenesis is a more sensitive factor than the measurement of an OCT scattering information or tumor thickness for predicting the risk of metastasis in melanoma, providing direct evidence of what could only be speculated in previous studies (Dadras et al., 2005, 2003). The following advantages of MFOCT have been shown: (i) the technique is capable of revealing the complete network structure of blood vessels and lymphatic vessels; (ii) lymphatic vessels and blood vessels can be visualized separately; (iii) the diameter of lymphatic vessels can be measured as an early biomarker of metastasis in response to tumor growth; (iv) dilatation of lymphatic duct can be identified earlier than the positive finding in PET and even before visual inspection of the tumor; and (v) as a noninvasive technique, MFOCT can scan the whole area of a primary tumor and the surrounding normal-appearing skin (rather than small area sampling in skin biopsy) to build a 3D information by a designed time course. The technique can also be used as an adjunct to histopathology in circumstances in which large areas must be examined, where apprehensive patients are screened, large populations are studied, or patients are regularly monitored.

MATERIALS AND METHODS

Melanoma mouse model and induction protocol

A breeding pair of B6.Cg-Braftm1Mmcm Ptentm1Hwu Tg(Tyr-Cre/ERT2)13Bos/BosJ mice (stock #013590) was purchased from the Jackson Laboratory (Bar Harbor, ME). We obtained Tyr::CreER; Braf^{CA}; Pten$^{lox/lox}$ mice from a breeding pair at the National Laboratory Animal Center (Tainan, Taiwan). Activation of CreER by 4-HT leads to melanocyte-specific conversion of *Braf*^{CA} to *Braf*^{V600E} and the conversion of *Pten*^{lox} alleles to null alleles (Dankort et al., 2009). For the topical treatment, 4-HT (H6278; Sigma-Aldrich, St. Louis, MO) was dissolved in 99.9% alcohol (32205; Sigma-Aldrich), and 1.5 mg/500 μl of 4-HT was administered to the dorsal part of both

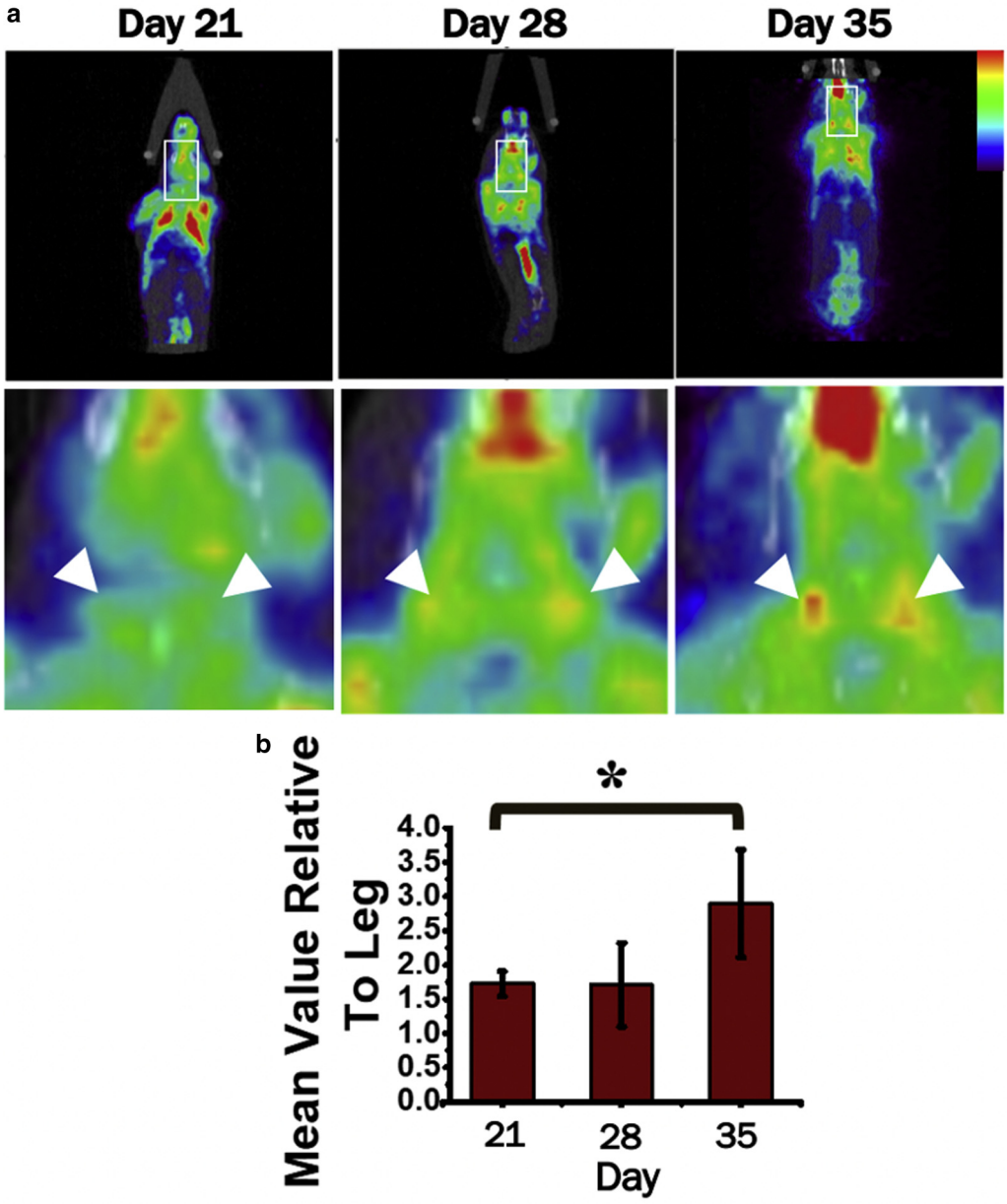

Figure 8. MicroPET-CT imaging and quantitative analysis in vivo. (**a**) Longitudinal 18 F-FDG microPET-CT images of a *Braf*$^{V600E/V600E}$;*Pten*$^{-/-}$ mouse. Details in the rectangular regions are enlarged. The white arrows point to the cervical LNs. (**b**) Mean uptake values in the cervical LNs relative to that in the leg versus time. Statistical significance was evaluated using the paired *t*-test. *$P < 0.05$. 18 F-FDG, ^{18}fluorodeoxyglucose; CT, computed tomography; LN, lymph node; PET, positron emission tomography.

ears on 10 occasions over 2 weeks (Chang et al., 2017). Melanoma was generated in the skin at a rate of 100% on day 42, and histopathology showed pigmented or nonpigmented S100-positive tumor cells in the dermis. These mice developed 100% neck LN metastasis by 56–70 days, which was the end of their survival.

Skin tissue processing and H&E and S100 staining

Skin tissues were fixed overnight in 10% neutral-buffered formalin at 4 °C and then transferred to 70% ethanol before being processed and embedded in paraffin. Paraffin-embedded specimens were cut into 5-μm sections and stained with H&E. Paraffin sections were deparaffinized and treated with antigen retrieval solution (citrate pH 6.0, Dako S236984) at 95 °C for 30 minutes, and 3% hydrogen peroxide in double-distilled water was used to block endogenous peroxidase activity. The primary antibody was applied with anti-S100 (1:500, ab868, Abcam, Cambridge, United Kingdom) at 4 °C overnight and was then incubated with secondary antibody at room temperature for 30 minutes. The signal was detected by AEC^{+} Substrate-Chromogen (Dako K346111). The sections were then counterstained with hematoxylin.

Imaging experiment design

We monitored the microenvironment changes of melanoma in the outer one third of each mouse ear once per week for 7 consecutive weeks. One to three regions per ear with less hair were selected to reduce image artifacts, and the areas easier to be fixed on the stage to minimize motion effects were chosen (Figure 9a, right). There were a total of 18 scanned areas (N = 18) in this study, 9 collected

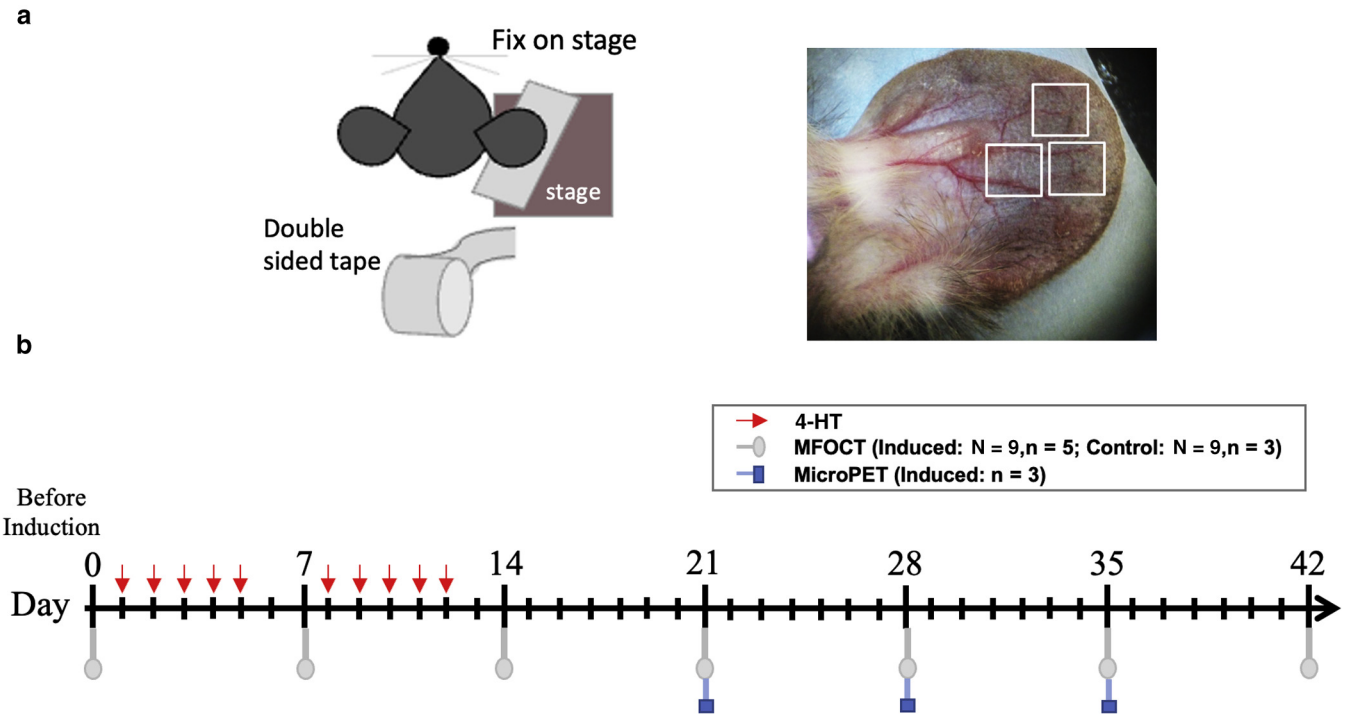

Figure 9. Experimental design. (**a**) Left: the cartoon indicates the stabilized procedure of a mouse ear lobe; right: photograph of a mouse ear. The scanned area is indicated with white squares. (**b**) Schematic of the experimental timeline. One to three regions per ear were chosen. Areas with less hair were selected to reduce image artifacts, and areas that were easier to be fixed on the stage were selected to reduce motion effects. N represents the number of scanned areas, and n represents the number of mice. 4-HT, (Z)-4-hydroxytamoxifen; MFOCT, multifunctional optical coherence tomography; PET, positron emission tomography.

from five *Braf* $^{V600E/V600E}$;*Pten*$^{-/-}$ mice and 9 collected from three *Braf* $^{CA/CA}$;*Pten*$^{loxp/loxp}$ mice. In the experimental timeline (Figure 9b), day 0 refers to the time point immediately before 4-HT treatment of mice began; after 7 days of 4-HT treatment, the time point was set as day 7; and so on. OCT images were obtained every week for both the *Braf* $^{V600E/V600E}$;*Pten*$^{-/-}$ and *Braf* $^{CA/CA}$;*Pten*$^{loxp/loxp}$ mice; microPET images (Gamma Medica-Ideas, Nortridge, CA) were obtained on days 21, 28, and 35 to confirm the timing of neck LN metastasis of melanoma. During the acquisition of OCT images, mice were anesthetized using 1% isoflurane, and the ears were fixed on the stage using double-sided tape. One adhesive side of the tape was fixed to the imaging stage, and the other side was fixed to the

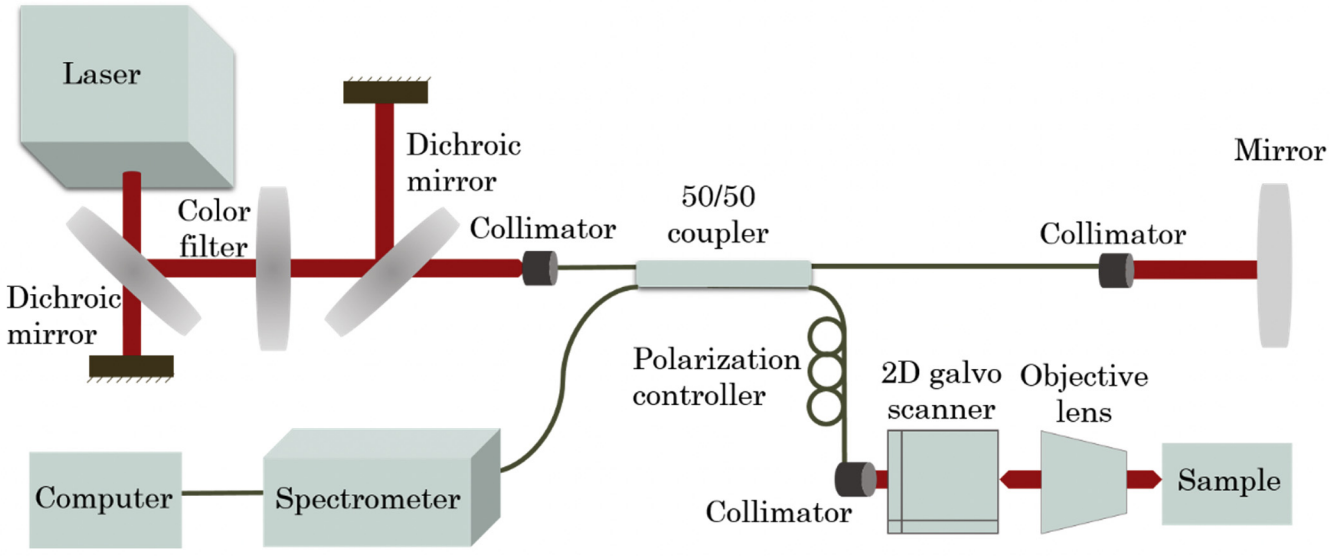

Figure 10. Setup of the MFOCT system. The light source of the MFOCT system has a central wavelength of 1,275 nm and a spectral bandwidth of 240 nm after passing through dichroic mirrors and a color filter. Then, the light was coupled into a fiber-based Michelson interferometer. The reference arm of the interferometer consisted of a mirror. The sample arm of the interferometer consisted of a dual-axis scanning mirror and an objective lens (Thorlabs, Newton, NJ). 2D, two-dimensional; MFOCT, multifunctional optical coherence tomography.

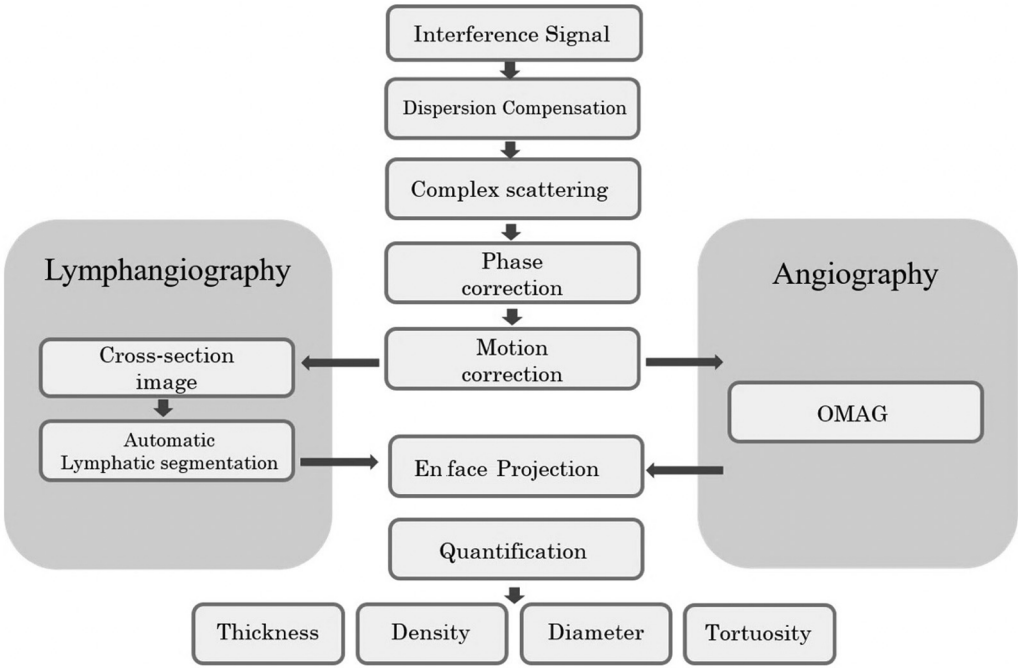

Figure 11. Flowchart of the MFOCT image processing. MFOCT, multifunctional optical coherence tomography; OMAG, optical microangiography algorithm.

mouse ear (Figure 9a, left). For longitudinal monitoring and relative comparison of the same area, the surface vascular features taken by photography were used as landmarks for registering the same region across time points. All animal procedures were reviewed and approved by the Institutional Animal Care and Use Committee of National Yang-Ming University, Taipei, Taiwan, where these experiments were performed.

MFOCT system

Figure 10 shows the setup of the MFOCT system (Kuo et al., 2016). The light source has a central wavelength of 1,275 nm and spectral bandwidth of 240 nm after passing through dichroic mirrors and a color filter, delivering an axial resolution of approximately 5 μm in air. Subsequently, the light is coupled to a fiber-based Michelson interferometer. The reference arm of the interferometer consists of a mirror. The sample arm of the interferometer comprises a dual-axis scanning mirror and an objective lens (Thorlabs, Newton, NJ), providing 7-μm lateral resolution. The x-scanner in the galvo system is steered using a saw-tooth waveform, and the y-scanner is steered using a step function. In this study, we obtained four repeated frames in each step, and each frame contained 900 A-lines. The 3D data set obtained consisted of 400 steps and covered an image volume of 4 × 4 × 2 mm^3. Backscattered light from the sample and reference arm was captured using a spectrometer. In our setup, the integration time of the camera in the spectrometer was set to 32.75 μs, and the imaging speed was 33 frames per second. Each 3D imaging took 50 seconds.

MFOCT signal processing

Figure 11 shows the procedure of the MFOCT signal processing. The dispersion was compensated using a numerical dispersion compensation algorithm (Wojtkowski et al., 2004), and axial signals were retrieved through the Fourier transform of the spectral interferogram. The complex scattering signal first underwent phase correction and motion correction in both axial and lateral directions (Lee et al., 2011). Simultaneously, the magnitude of the complex number was calculated to construct cross-sectional images.

OCT angiography was determined using the optical microangiography algorithm (Wang, 2010). OCT angiography is a technique to generate in vivo vascular images using endogenous motion contrast. It can distinguish the moving particles from the static tissue, generate flow signals, and allow the visualization of microvascular networks in biological tissues without a need for intravenous dye injection. The optical microangiography algorithm we used to calculate OCT angiography has been proven valid using multiphoton microscopy (Wang et al., 2014). Because the lymphatic vessels scattered less light than the mouse ear tissue, lymphangiography can be identified through the automatic lymphatic segmentation of weakly scattering areas in the cross-sectional image, using our recently proposed method (Lai et al., 2020) where an in vivo fluorescence lymphangiography was used for validation.

Quantitative analysis

We measured the ear thickness for quantitative analysis, which was defined as the distance between the corneum stratum and articular cartilage. The top boundary and the dermis–cartilage junction were determined using the method described in the literature (Lai et al., 2020). Operator-dependence manual boundary–determined steps were not necessary. Three parameters—vessel density, vessel diameter, and the tortuosity of lymphatic and blood vessels—were also automatically calculated using a program written in MATLAB and were used to assess microenvironment changes in $Braf^{V600E/V600E}$;$Pten^{-/-}$ and $Braf^{CA/CA}$;$Pten^{loxp/loxp}$ mouse ears.

The vessel density is defined as the area of the vessels in the projection view divided by the area of the imaging region. Using the Euclidean distance transform of the binarized vessel en face projection map, the distance between each pixel in a binarized map and the pixel locations that approximate the centerline of the blood vessels (i.e., vessel skeleton) can be counted in pixel number and then averaged as the median vessel diameter. Vessel tortuosity was

determined by calculating the entropy of the skeletonized vessel en face projection map. Larger tortuosity entropy corresponds to a more tortuous and wavier vessel trajectory (Chen et al., 2018).

Statistical analysis

Two-sample *t*-tests (two-sided) were used to compare the treatment and control samples. In comparing the same area at the different time points in the control and induced groups, the paired *t*-tests were used. Given that microcirculation's condition varies from mouse to mouse and even varies from a different region in the same ear, we calculated a relative (%) increase in the same region across different time points. To explore the effect of different scanned areas on OCT quantitative analysis at each time point, the linear mixed model was performed using the Statistical Package for the Social Sciences software (SPSS 24, IBM, Armonk, NY). The linear mixed model analysis confirmed no significant difference in OCT angiography and lymphangiography among different scan areas at each time point.

Data availability statement

No datasets were generated or analyzed during this study.

ORCIDs

Pei-Yu Lai: https://orcid.org/0000-0002-5176-3935
Tai-Yu Shih: https://orcid.org/0000-0002-4383-8343
Yu-Huan Chang: https://orcid.org/0000-0001-6999-9084
Ya-Shuan Chou: https://orcid.org/0000-0002-0462-895X
Ting-Hua Wu: https://orcid.org/0000-0003-0501-7162
Yu-Ya Su: https://orcid.org/0000-0002-6457-2003
Chung-Hsing Chang: https://orcid.org/0000-0003-2197-4923
Wen-Chuan Kuo: https://orcid.org/0000-0001-7432-1948

AUTHOR CONTRIBUTIONS

Conceptualization: WCK, CHC; Data Curation: PYL, TYS, YHC, YSC, THW, YYS; Formal Analysis: PYL, TYS, YHC; Funding Acquisition: WCK, CHC; Investigation: PYL, TYS, YHC, YSC, THW, YYS, WCK, CHC; Methodology: WCK, CHC; Project Administration: WCK, CHC; Resources: WCK, CHC; Software: PYL; Supervision: WCK, CHC; Validation: PYL, WCK, CHC; Visualization: PYL, WCK, CHC; Writing - Original Draft Preparation: PYL; Writing - Review and Editing: WCK, CHC

ACKNOWLEDGMENTS

This research was supported, in part, by the Ministry of Science and Technology (MOST), Taiwan 109-2112-M-010-002 (WCK) and 107-21 2314-B-303-010-MY3 (CHC, the co-corresponding author of this study. E-mail: miriamchangch@gmail.com).

CONFLICT OF INTEREST

The authors state no conflict of interest.

REFERENCES

Baran U, Qin W, Qi X, Kalkan G, Wang RK. OCT-based label-free in vivo lymphangiography within human skin and areola. Sci Rep 2016;6:21122.

Bohren CF, Huffman DR. Absorption and scattering of light by small particles. Weinheim, Germany: John Wiley & Sons; 1983.

Borda LJ, Wikramanayake TC. Seborrheic dermatitis and dandruff: a comprehensive review. J Clin Investig Dermatol 2015;3. https://doi.org/10.13188/2373-1044.1000019.

Cadili A, Dabbs K. Predictors of sentinel lymph node metastasis in melanoma. Can J Surg 2010;53:32–6.

Chang CH, Kuo CJ, Ito T, Su YY, Jiang ST, Chiu MH, et al. CK1α ablation in keratinocytes induces p53-dependent, sunburn-protective skin hyperpigmentation. Proc Natl Acad Sci USA 2017;114:E8035–44.

Chen PH, Wu CH, Chen YF, Yeh YC, Lin BH, Chang KW, et al. Combination of structural and vascular optical coherence tomography for differentiating oral lesions of mice in different carcinogenesis stages. Biomed Opt Express 2018;9:1461–76.

Dadras SS, Lange-Asschenfeldt B, Velasco P, Nguyen L, Vora A, Muzikansky A, et al. Tumor lymphangiogenesis predicts melanoma metastasis to sentinel lymph nodes. Mod Pathol 2005;18:1232–42.

Dadras SS, Paul T, Bertoncini J, Brown LF, Muzikansky A, Jackson DG, et al. Tumor lymphangiogenesis: a novel prognostic indicator for cutaneous melanoma metastasis and survival. Am J Pathol 2003;162:1951–60.

Dankort D, Curley DP, Cartlidge RA, Nelson B, Karnezis AN, Damsky WE Jr, et al. Braf(V600E) cooperates with Pten loss to induce metastatic melanoma. Nat Genet 2009;41:544–52.

Dieterich LC, Detmar M. Tumor lymphangiogenesis and new drug development. Adv Drug Deliv Rev 2016;99:148–60.

Doeden K, Ma Z, Narasimhan B, Swetter SM, Detmar M, Dadras SS. Lymphatic invasion in cutaneous melanoma is associated with sentinel lymph node metastasis. J Cutan Pathol 2009;36:772–80.

Eklund L, Bry M, Alitalo K. Mouse models for studying angiogenesis and lymphangiogenesis in cancer. Mol Oncol 2013;7:259–82.

Emmett MS, Symonds KE, Rigby H, Cook MG, Price R, Metcalfe C, et al. Prediction of melanoma metastasis by the Shields index based on lymphatic vessel density. BMC Cancer 2010;10:208.

Gashev AA, Nagai T, Bridenbaugh EA. Indocyanine green and lymphatic imaging: current problems. Lymphat Res Biol 2010;8:127–30.

Gong P, McLaughlin RA, Liew YM, Munro PR, Wood FM, Sampson DD. Assessment of human burn scars with optical coherence tomography by imaging the attenuation coefficient of tissue after vascular masking. J Biomed Opt 2014;19:21111.

Kim WB, Jerome D, Yeung J. Diagnosis and management of psoriasis. Can Fam Physician 2017;63:278–85.

Kuo WC, Kuo YM, Wen SY. Quantitative and rapid estimations of human subsurface skin mass using ultra-high-resolution spectral domain optical coherence tomography. J Biophotonics 2016;9:343–50.

Lai PY, Chang CH, Su HR, Kuo WC. Lymphatic vessel segmentation in optical coherence tomography by adding U-Net-based CNN for artifact minimization. Biomed Opt Express 2020;11:2679–93.

Leachman SA, Cassidy PB, Chen SC, Curiel C, Geller A, Gareau D, et al. Methods of melanoma detection. Cancer Treat Res 2016;167:51–105.

Lee J, Srinivasan V, Radhakrishnan H, Boas DA. Motion correction for phase-resolved dynamic optical coherence tomography imaging of rodent cerebral cortex. Opt Express 2011;19:21258–70.

Massi D, Puig S, Franchi A, Malvehy J, Vidal-Sicart S, González-Cao M, et al. Tumour lymphangiogenesis is a possible predictor of sentinel lymph node status in cutaneous melanoma: a case-control study. J Clin Pathol 2006;59:166–73.

McMasters KM, Wong SL, Edwards MJ, Ross MI, Chao C, Noyes RD, et al. Factors that predict the presence of sentinel lymph node metastasis in patients with melanoma. Surgery 2001;130:151–6.

McPherson T. Current understanding in pathogenesis of atopic dermatitis. Indian J Dermatol 2016;61:649–55.

Morton DL, Hoon DS, Cochran AJ, Turner RR, Essner R, Takeuchi H, et al. Lymphatic mapping and sentinel lymphadenectomy for early-stage melanoma: therapeutic utility and implications of nodal microanatomy and molecular staging for improving the accuracy of detection of nodal micrometastases. Ann Surg 2003;238:538–50.

Munn LL, Padera TP. Imaging the lymphatic system. Microvasc Res 2014;96:55–63.

Paek SC, Griffith KA, Johnson TM, Sondak VK, Wong SL, Chang AE, et al. The impact of factors beyond Breslow depth on predicting sentinel lymph node positivity in melanoma. Cancer 2007;109:100–8.

Pomerantz R, Zell D, McKenzie G, Siegel DM. Optical Coherence Tomography Used as a Modality to Delineate basal cell carcinoma prior to Mohs Micrographic Surgery. Case Rep Dermatol 2011;3:212–8.

Qin W, Baran U, Wang R. Lymphatic response to depilation-induced inflammation in mouse ear assessed with label-free optical lymphangiography. Lasers Surg Med 2015;47:669–76.

Rainer BM, Kang S, Chien AL. Rosacea: epidemiology, pathogenesis, and treatment. Dermatoendocrinol 2017;9:e1361574.

Rhodes AR, Melski JW, Sober AJ, Harrist TJ, Mihm MC Jr, Fitzpatrick TB. Increased intraepidermal melanocyte frequency and size in dysplastic melanocytic nevi and cutaneous melanoma. a comparative quantitative study of dysplastic melanocytic nevi, superficial spreading melanoma, nevocellular nevi, and solar lentigines. J Invest Dermatol 1983;80:452–9.

Seo MJ, Lee JJ, Kim HO, Chae SY, Park SH, Ryu JS, et al. Detection of internal mammary lymph node metastasis with (18)F-fluorodeoxyglucose positron emission tomography/computed tomography in patients with stage III breast cancer. Eur J Nucl Med Mol Imaging 2014;41:438–45.

Shayan R, Karnezis T, Murali R, Wilmott JS, Ashton MW, Taylor GI, et al. Lymphatic vessel density in primary melanomas predicts sentinel lymph node status and risk of metastasis. Histopathology 2012;61:702–10.

Storr SJ, Safuan S, Mitra A, Elliott F, Walker C, Vasko MJ, et al. Objective assessment of blood and lymphatic vessel invasion and association with macrophage infiltration in cutaneous melanoma. Mod Pathol 2012;25:493–504.

Streit M, Detmar M. Angiogenesis, lymphangiogenesis, and melanoma metastasis. Oncogene 2003;22:3172–9.

Takenaka T, Yano T, Morodomi Y, Ito K, Miura N, Kawano D, et al. Prediction of true-negative lymph node metastasis in clinical IA non-small cell lung cancer by measuring standardized uptake values on positron emission tomography. Surg Today 2012;42:934–9.

Thomas L, Tranchand P, Berard F, Secchi T, Colin C, Moulin G. Semiological value ABCDE criteria diagnosis cutaneous pigmented tumors. Dermatology 1998;197:11–7.

Turani Z, Fatemizadeh E, Blumetti T, Daveluy S, Moraes AF, Chen W, et al. Optical radiomic signatures derived from optical coherence tomography images to improve identification of melanoma. Cancer Res 2019;79:2021–30.

Vakoc BJ, Lanning RM, Tyrrell JA, Padera TP, Bartlett LA, Stylianopoulos T, et al. Three-dimensional microscopy of the tumor microenvironment in vivo using optical frequency domain imaging. Nat Med 2009;15:1219–23.

Wang H, Baran U, Li Y, Qin W, Wang W, Zeng H, et al. Does optical microangiography provide accurate imaging of capillary vessels?: validation using multiphoton microscopy. J Biomed Opt 2014;19:106011.

Wang RK. Optical microangiography: a label free 3D imaging technology to visualize and quantify blood circulations within tissue beds in vivo. IEEE J Sel Top Quantum Electron 2010;16:545–54.

Welzel J, Bruhns M, Wolff HH. Optical coherence tomography in contact dermatitis and psoriasis. Arch Dermatol Res 2003;295:50–5.

Wojtkowski M, Srinivasan VJ, Ko TH, Fujimoto JG, Kowalczyk A, Duker J. Ultrahigh-resolution, high-speed, Fourier domain optical coherence tomography and methods for dispersion compensation. Opt Express 2004;12:2404–22.

Yousefi S, Zhi Z, Wang RK. Label-free optical imaging of lymphatic vessels within tissue beds in vivo. IEEE J Sel Top Quantum Electron 2014;20:6800510.